

See discussions, stats, and author profiles for this publication at: <https://www.researchgate.net/publication/46382479>

On the origin of an unusual dependence of (bio)chemical reactivity of ferric hydroxides on nanoparticle size

ARTICLE *in* PHYSICAL CHEMISTRY CHEMICAL PHYSICS · NOVEMBER 2010

Impact Factor: 4.49 · DOI: 10.1039/c0cp00168f · Source: PubMed

CITATIONS

18

READS

17

3 AUTHORS:



Irina V Chernyshova

Columbia University

41 PUBLICATIONS 688 CITATIONS

SEE PROFILE



Sathish Ponnuram

Columbia University

15 PUBLICATIONS 85 CITATIONS

SEE PROFILE



Ponisseril Somasundaran

Columbia University

535 PUBLICATIONS 11,755 CITATIONS

SEE PROFILE

On the origin of an unusual dependence of (bio)chemical reactivity of ferric hydroxides on nanoparticle size†

I. V. Chernyshova,* S. Ponnuram and P. Somasundaran

Received 9th April 2010, Accepted 17th August 2010

DOI: 10.1039/c0cp00168f

Application of *in situ* UV-Vis absorption spectroscopy and *ex situ* X-ray photoelectron spectroscopy (XPS) makes it possible to resolve the controversies about the electronic properties of hematite (α -Fe₂O₃) nanoparticles (NPs) and, on this basis, to rationalize the unusual dependence of aquatic (bio)chemistry of these NPs on NP size. 2-Line ferrihydrite (FH) is also included in the study as the end polymorph of the size-driven phase transformation of hematite NPs in aqueous media. It is shown that the absorption edge of all NPs studied is due to the direct O 2p–Fe 3d charge transfer (CT) process, while a manifold of weak bands superimposed onto two main p–d CT bands is attributed to the d–d ligand field transitions. The band gap decreases from 2.95 to 2.18 eV with increasing NP size from 7 nm to 120 nm. This effect is attributed to restoration of hematite lattice structure, which ultimately results in an increase in the O 2p–Fe 3d hybridization, stabilization of the valence band, and delocalization of valence electrons, as confirmed by XPS. Finally, we show that the optical effects such as the Mie resonance significantly distort absorption spectra of hematite NPs larger than \sim 120 nm. Possible impacts of these findings on (photo)catalytic and biochemical properties of ferric (hydr)oxide NPs are discussed.

Introduction

Ferric (hydr)oxide nanoparticles (NPs) have attracted much attention because they are abundant in both living organisms and the environment and also are of great technological interest due to their special physicochemical and electronic properties, low processing and synthesis costs, and environmental compatibility.^{1–4} These NPs exhibit an unusual dependence of their (bio)chemical properties on particle size: the surface-area/adsorption-normalized oxidative catalytic⁵ and photocatalytic^{6–8} activity as well as hydrogen-generation efficiency⁹ of hematite (α -Fe₂O₃) decrease with decreasing size of NPs. The same size-dependent trend was recently reported for redox activity of goethite (α -FeOOH).¹⁰ The reduction rate of hematite NPs by the dissimilatory iron reducing bacteria, *Shewanella oneidensis* MR-1, also significantly decreases with decreasing NP size.¹¹ Hydrated ferric oxide/hematite NPs with a maximum diameter of about 7.5 nm, which constitute an inner core of ferritin (an iron storage protein), are biocompatible. However, 70 nm hematite was found to be cytotoxic.¹² Adsorption capacity of goethite¹³ towards both anions and cations decreases with decreasing size of NPs. Both adsorption affinity and adsorption capacity of hematite NPs also diminish with decreasing NPs, as seen from the reported adsorption data^{6,14,15} normalized

with respect to the NP surface (Fig. S1, ESI†). Such a trend is rather counterintuitive since smaller NPs with higher fraction of surface atoms — in the coordination environments different from that of the corresponding ideally-terminated surface planes — are commonly associated with higher reactivity.^{16–18} For example, both adsorption¹⁶ and reduction¹⁹ capacity of magnetite (Fe₃O₄) significantly increase for NP sizes smaller than 20 nm. Photocatalytic activity of anatase increases with decreasing NP size down to 7–25 nm.¹⁶ Similarly, smaller ZnO NPs are more effective in photodegradation of dyes.²⁰ This leads to a puzzle not yet addressed: What are the mechanisms behind such “anomalous” aquatic chemistry of ferric (hydr)oxides?

A common approach to searching for an answer to this question would be to focus on understanding changes in the molecular structure of the NP–solution interface.²¹ However, to uniquely identify molecular-level events and structures responsible for reactivity of surfaces in aqueous systems presents a serious problem, despite the recent progress in the instrumental and computational methods.²² At the same time, from a fundamental standpoint, such intrinsic properties of NPs as bond stability, adsorption affinity, and conductivity and hence acid–base, redox, and (photo)catalytic properties are controlled by their electronic structures,²³ which is reflected in surface free energy and specific surface functionalities. Then, addressing changes in the electronic properties of the NPs in water can lead to determining the driving forces of their aquatic chemistry, which is pivotal for defining strategies to tune technological performance of the NPs.

In this study, we focus on hematite as its case is special: The dependence of its (bio)chemical reactivity on NP size is observed at sizes larger than 10 nm, *i.e.*, in the size range where neither the quantum confinement (QC) nor surface

NSF I/UCRC Center for Particulate & Surfactant Systems (CPaSS), Columbia University, New York, 10027 NY, USA.
E-mail: irina905c@gmail.com

† Electronic supplementary information (ESI) available: Literature data on the NP size effect on adsorption properties of hematite, NP synthesis details, morphological characteristics of NPs, experimental and TS theoretical positions as well as assignment of bands in UV-Vis absorption spectra of aqueous suspensions of hematite NPs, O 1s XPS spectra, O/Fe atomic concentration ratios of NPs calculated using areas of O 1s and Fe 2p_{3/2} XPS peaks. See DOI: 10.1039/c0cp00168f

curvature effects are expected.^{18,24–27} Hence, the reason for this dependence is likely to be size-induced changes of the NP structure. In fact, bulk hematite has corundum structure with octahedrally coordinated ferric cations. Though this mineral is the most stable iron (hydr)oxide polymorph under oxidizing conditions,¹ in the nanosize regime it possess tetrahedral defects in the near-surface region.²⁸ Concentration of such defects increases with decreasing NP size, suggesting that hematite is destabilized with respect to ferrihydrite in aqueous media.²⁸ However, it is a challenge to mechanistically relate these structural changes to the variations in the interfacial reactivity of hematite NPs since actual lattice and electronic structures of the intermediate and end states of the phase transformation are as-yet poorly understood or unknown.

Even fundamental electronic characteristics of hematite NPs such as the nature of the insulating band gap and the change of the band gap with NP size remain controversial. In fact, the optical band gap of hematite (typically of 1.9–2.3 eV) has previously been described by two competing models. One is the O 2p → Fe 3d ligand to metal charge transfer (CT) direct band gap. This model follows from the X-ray^{29–33} and UV-Vis^{34–43} spectroscopic and theoretical^{44–47} studies. It suggests that holes have the O 2p character, while the minimum of the conduction band is positioned in momentum (*k*) space directly under the maximum of the highest valence band and hence both the charge transfer and the electron–hole recombination are not mediated by phonons.⁴⁸ If so, the mismatch between the absorption and photoresponse spectra of nanoparticulate hematite photoelectrodes, which consists in the steeper onset of the former compared to the latter (see examples in ref. 35,36,49–52) can be attributed^{51,53} to longer penetration depths of less energetic photons. This in turn results in a higher probability of the generated holes to be trapped and/or annihilated before reaching the hematite–solution interface. However, the CT direct band gap fails to explain several important facts. Namely, it is unclear why fluorescence is quenched by coarse hematite particles but is observed for NPs,⁵⁴ given the direct band-gap semiconductors are generally fluorescent.⁴⁸ Also, the O 2p character suggests that holes in hematite are delocalized, which contradicts to their intrinsically low mobility.^{51,55}

The alternative model associates the absorption edge with the Fe 3d → Fe 3d ligand field (LF) intraband electronic transitions, namely, to the double exciton process (DEP) resulting from the coupling of two adjacent octahedrally-coordinated Fe³⁺ cations.^{1,49,50,53,56–61} The LF transitions are indirect (phonon-assisted)⁴⁸ and hence less absorptive than the direct CT transitions.^{57,62–65} This model is consistent with both the size dependence of fluorescence and the low mobility of holes. In fact, as NP size decreases, the LF transitions become progressively forbidden^{56,58,66–68} due to the weakening of superexchange interactions associated with the NP-size driven decrease in trigonal distortion of the ferric octahedra.^{3,69} As a result, the direct O 2p → Fe 3d CT transitions start to progressively dominate at the absorption edge, which ultimately activates spontaneous emission. Holes generated through the LF excitations have the Fe⁴⁺ character. They are highly localized in the narrow d bands and hence have low intrinsic mobility.⁷⁰ In addition, the difference between the

absorption and photoresponse spectra of nanoparticulate hematite can be attributed to lower oxidizing capacity of the Fe⁴⁺ holes compared to the O[−] counterparts.^{50,57} However, the LF indirect band gap model also suffers from a number of drawbacks. If Fe⁴⁺ were to appear within the interior of hematite NPs, it is expected to extract electron from the O 2p valence band rather than remain in the +4 valence state, because the O 2p–Fe 3d charge transfer energy is lower than the d–d correlation energy.^{30,33,34} Furthermore, the applicability of the LF concept to hematite can also be challenged based on the fact that there is no abrupt change in the quantum efficiency near the boundary between the O 2p–Fe 3d charge transfer and LF transitions.^{51,53} Finally, the DEP band at 2.3–2.5 eV was recently attributed to dipole-forbidden p–d CT transition $t_{1g} \rightarrow t_{2g}$.³⁴

The currently available experimental data on the NP size effect on the energy gap are also contradictory. Specifically, a hypochromic shift of the absorption edge of hematite with decreasing NP size has been found in most studies and been related to QC,^{9,52,56,60,71–73} though a more recent study related this effect to a decrease of the trigonal crystal lattice distortion.⁷⁴ At the same time, bathochromic⁷⁵ and no shift⁵⁹ has recently been observed and considered as a proof of the CT and LF insulating gaps, respectively. Finally, there is no consensus about the NP size effect on covalency of the Fe–O bonds of hematite. Though a decrease in NP size has been found to enhance both d–p hybridization and valence electron delocalization,^{54,76} the opposite trend has also been observed.^{59,71}

In summary, a systematic study of changes in the electronic properties of hematite NPs with NP size can help in simultaneously achieving two goals. The first is to obtain the basic insights into the unusual dependence of the chemical properties of hematite on the NP size. The second is to resolve the band gap dilemma because the different types of electronic transitions are to be affected in a different way or extent by the size-induced distortions of the hematite lattice structure. These objectives can be achieved using UV-Vis absorption and X-ray photoelectron spectroscopies (XPS), which are the main tools in assessing the optical band gap and probing the electronic structures of NPs, respectively. However, in the case of NPs with high refractive indexes,[‡] the optical method can suffer from the optical distortions that are caused by scattering and interference of radiation by NPs.⁷⁷ These optical effects, which can be one of the sources of the aforementioned contradictions, have generally been overlooked in the previous studies. Herein, we apply UV-Vis optical spectroscopy under conditions when the optical distortions are minimal. As samples, we use highly monodisperse and pure hematite NPs with similar aspect ratios. Some of these samples were employed in our studies of the redox properties of hematite NPs,⁵ which enables a direct structure–property correlation. For comparison, 2-line ferrihydrite (FH) is also studied as a proxy surface of hydrated hematite NPs smaller than 40 nm which experience gradual phase transformation to FH.²⁸ FH is a low-crystalline, cation-deficient ferric (hydr)oxide (its composition in the more

‡ Hematite belongs to this category as its refractive index is as high as 2.9–2.7.

ordered form is $\text{Fe}_{10}\text{O}_{14}(\text{OH})_2 + \sim \text{H}_2\text{O}$ which contains both tetrahedrally and octahedrally coordinated ferric ions.^{78,79} We found that the band gap of hematite NPs is monotonically enlarged with decreasing NP size due to the size-driven distortions of the hematite structure. We also show that the Mie resonance significantly distorts absorption spectra of hematite NPs larger than ~ 120 nm. These results are very important and practically useful since they are able to shed light on the dependence of the (photo)chemical and biochemical properties of ferric (hydr)oxides on NP size.

Experimental

All chemicals were of pure-for-analysis grade or higher and solutions were prepared from triply distilled water (TDW). All glassware and high-density polyethylene (HDPE) containers were rinsed with 0.1 M HNO_3 and TDW before use. Hematite NPs of mean TEM sizes of 7, 9, 30, 38, 45, 60, and 120 nm were synthesized by forced hydrolysis, while 150 nm hematite and FH were commercial (ESI[†]).

The NPs were characterized by transmission electron transmission microscopy (TEM), X-ray diffraction (XRD), and BET surface area measurements. TEM was performed on a Jeol JEM 100CX Transmission Electron Microscope (TEM) operated in the bright field mode at 100 keV. X-Ray diffractograms were recorded using a Scintag Model X2 X-ray powder diffractometer. A $\text{CuK}\alpha$ ($\lambda = 0.154$ nm) radiation source operated at 45 kV and 35 mA was used. The scan step size was 0.05° . Estimates of the surface area were made with a single-point BET N_2 adsorption isotherm obtained using a Monosorb (Quantachrome) surface area analyzer. The samples were degassed at 50°C for 30 min before measurements were taken. Two or three replicate measurements were performed, which gave results that agreed within less than 5%.

UV-Vis absorption spectra were measured on suspensions of NPs in TDW using Lambda-25 (Perkin-Elmer) spectrophotometer at the scan speed of 120 nm min^{-1} and a 1 nm slit. Spectra were run immediately after sonicating the suspensions for 1 h, in 1 cm quartz cuvettes.

XPS spectra were collected with a Perkin-Elmer PHI 5500 instrument using monochromatic $\text{AlK}\alpha$ X-rays with pass energies of 17.6 eV at resolution of 0.9 eV, at take-off angle of 45° , at pressures of less than 1×10^{-8} Torr, calibrated using the Ag 3d peak. Scans of X-ray induced Auger peaks were performed at 0.1 eV steps. All samples were prepared by spreading a thin layer of an aqueous suspension of NPs on a UHV metallic holder followed by air-drying.

Results

Characterization by TEM, BET surface area, XRD, and XPS

Morphology and size of the NPs were characterized using TEM (Fig. 1 and Table S1, ESI[†]). The samples are labeled according to mean NPs size as measured by averaging sizes of 10–15 NPs. FH NPs are strongly agglomerated. Shape and size of the primary FH NPs cannot be resolved by the instrument used. Reported crystal size of 2-line FH is about 2 nm,^{80,81} while the extension range of local structural order is

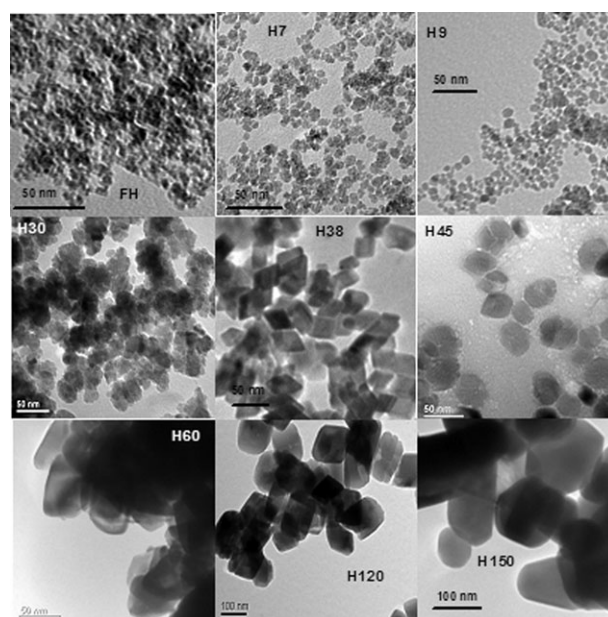


Fig. 1 TEM images of hematite NPs.

as low as 4 \AA .⁸⁰ H7 and H9 hematite NPs exhibit average diameter of 7.0 ± 0.5 and 9 ± 1 nm, respectively, and a rounded irregular hexagonal shape as viewed along the optical axis of the microscope. H30 have agglomerate-like irregular shape and average diameter of ~ 30 nm. These globules are porous, which is confirmed by the fact that their geometrical surface area (GSA) is smaller than the BET value (Table S1, ESI[†]). H38 NPs have well developed rhombohedral shape. Examination of the TEM image does not reveal pores on the surface of H38 NPs and gives their average diameter of 38 ± 5 nm. The GSA value for H38 matches the BET surface area within the experimental error, confirming that H38 NPs are non-porous. H45 and H60 NPs have rounded rhombohedral shape and a comparison of the GSA and BET values (Table S1, ESI[†]) reveals them to be porous. H120 are rhombohedral, while H150 NPs are rounded polyhedral. Both H120 and H150 are highly monodisperse and non-porous. Aspect ratio of the NPs used in this study is similar (ranging from 1 to 2). All the samples were tested for the presence of surface impurities using XPS. In addition to adventitious carbon, only ferric iron and oxygen were detected on hematite NPs, while FH was found to contain Si at the Si/Fe atomic ratio of 0.025.

The phase identity of hematite NPs and FH used in this study was verified by XRD (Fig. 2). The diffractogram of FH is dominated by two broad lines characteristic of 2-line FH. There are also minor peaks which point to the presence of a small admixture of hematite phase in FH. Except for H7, all the hematite NPs show only hematite diffraction patterns, with no lines due to other impurity phases. H7 has some admixture of 6-line ferrihydrite. For all hematite NPs, the (110) and (300) lines are sharper than lines (104), (018), (202), and (024). It follows that hematite NPs have either plate-like shape with an excess of the planes (near) perpendicular to the c axis or better developed basal facets. The XRD lines gradually sharpen as NP size increases, which is a signature of an increase in the average crystallinity size. The latter was quantified using the

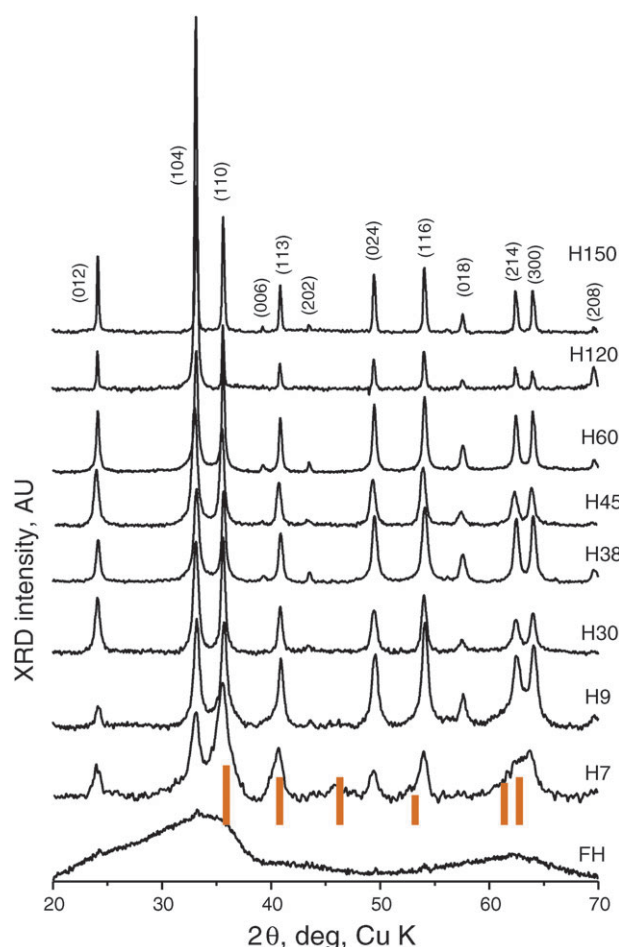


Fig. 2 XRD patterns of hematite NPs. Bars show XRD pattern of 6-line ferrihydrite (JCPDS card #86-0550).

Scherrer formula with a shape factor of 1 after removing the instrumental broadening by simple subtraction. The instrumental broadening was taken as the line widths in the XRD pattern of micron-size natural hematite. The values of the mean coherence length extracted from the widths of the (104) and (110) lines (Table S2, ESI†) show that the TEM size is close to the average crystallite size for H7, H30, H38, and H60. At the same time, H9 in the dried state became ~20–25 nm size (confirmed by remeasurement of primary particle size using TEM of the dried-redispersed NPs). The growth upon air drying implies high instability of the 9 nm hematite. On the other hand, smaller, 7 nm, NPs are stable, which can be attributed to the presence of a larger amount of the FH phase. In contrast to the other NPs, the crystallite size of H45 is ~30 nm, implying that these NPs are polycrystalline.

Comparison of relative intensities of XRD lines shows, with several exceptions due to the texture effects, that intensities of the (024), (300) and (116) XRD lines relative to that of the Fe-independent (113) line decrease in the following descending order: H38 > H60 > H150 ≈ H120 > H45 > H9 > H20 > H7.

It follows that disorder in the Fe sublattice of hematite, which was previously attributed to Fe vacancies associated with structural OH impurities,⁸² is not a simple function of NP

size. Indeed, the XPS analysis (Fig. S3a, ESI†) shows that, compared to the other NPs, H38 and H7 are characterized by the minimum and maximum of relative concentration of defective lattice oxygen, respectively. The minimum concentration of oxygen defects in H38 can temporarily be assigned to the peculiarities of its morphology (Fig. 1). At the same time, relative concentration of the regular lattice oxygen decreases with decreasing NP size (Fig. S3b, ESI†), as is expected for NPs synthesized in water.¹

Size dependence of UV-Vis absorption spectra of hematite NPs in aqueous suspensions

For analysis, UV-Vis absorption spectra were normalized either by intensity of the most intense band (Fig. 3a and b) or by concentration of NPs in g l^{-1} (Fig. 3c). In the latter case, with exception for the spectrum of H150 which exhibits strong optical distortions (*vide infra*), the spectra were also partially corrected for scattering. Namely, a linear baseline was subtracted, which was drawn by extrapolating a slope in the 700–1100 nm range towards 190 nm. This approach underestimates contribution of scattering at short wavelengths λ , which increases as $1/\lambda^n$, where $n = 4.25\text{--}5$ for hematite NPs up to 100 nm size in air,^{42,83} but minimizes it in the absorption edge area. Spectra of hematite NPs from 7 to 60 nm size (Fig. 3) are consistent with previously reported absorption spectra of nanoparticulate hematite.^{42,49,58,74,84–87} The spectrum of H7 consists of the main absorption band (marked as CT1) at ~195 nm with weak features at ~300 and 365 nm. As particle size increases,§ the CT1 band monotonically red shifts, while its relative intensity decreases. In contrast, the 365 nm feature (marked as CT2) red shifts but increases in intensity, becoming dominant in the absorption of 120 nm particles. In addition, an increase in NP size also gives rise to a series of weaker bands, marked with integers from 1 to 7 in Fig. 3. The spectrum of H120 differs from spectra of H7 and H9 but is very similar to the absorption⁵⁸ and energy losses spectra^{34,42,88,89} of well-crystallized hematite.

The spectrum of H150 significantly differs from that of H120. The former is characterized by (1) an anomalously higher intensity and lower energy of the CT2 band, (2) a more gradual absorption edge, which cannot be assigned to higher concentration of structural impurities in H150 according to the XRD and vibrational spectroscopy analysis, and (3) an increased scattering. Such an irregular spectral pattern is well known in optics and is attributed to the Mie resonance.^{83,90,91} This effect is a cavity resonance which appears in the optical spectra of particles at a certain combination of the wavelength, complex refractive index of the particle, and particle size. It is most pronounced in the spectral region where the imaginary part of the absorption index is small.⁹⁰ For hematite, these conditions are $\lambda > 500$ nm and particle size (in water) larger than ~100 nm.⁸³

Below we address assignment of the CT1 and CT2 bands. There is consensus that the CT1 band is due to the electric dipole allowed ligand-to-metal charge transfer (CT) transitions from O 2p to Fe^{3+} 3d orbitals.^{58,86} However, the CT2 band has been attributed to the CT as well as LF transitions

§ Size of H45 is taken to be equal to its crystallite size of 30 nm.

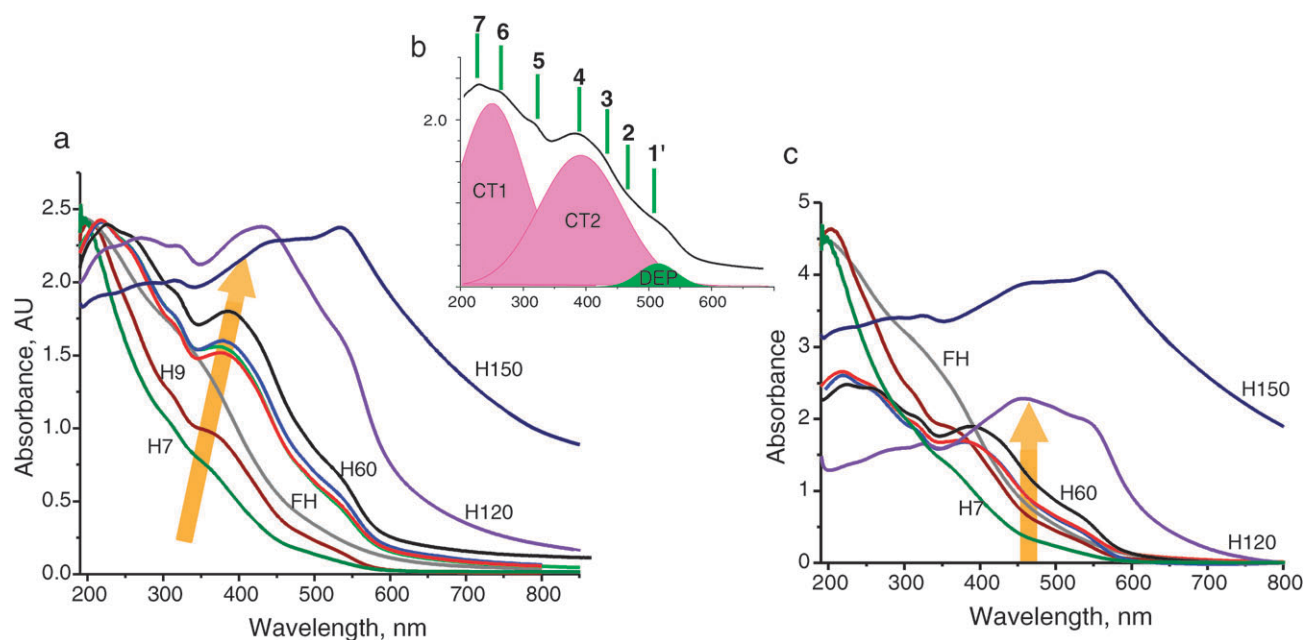


Fig. 3 UV-Vis absorption spectra of aqueous suspensions of FH and hematite NPs: (a) normalized by maximum band intensity; (b) positions of two charge transfer bands CT1 and CT2 as well as ligand field bands (DEP and bands 1'–7) in spectrum of H60; (c) spectra normalized to concentration of NPs of 0.1 g l^{-1} and partial correction for scattering except for H150 (see text for details). From bottom to top as indicated by arrow: H7 (olive), H9 (wine), FH (grey), H30 (red), H45 (green), H38 (blue), H60 (black), H120 (violet), and H150 (navy).

(Table S2, ESI†). There are the two main objections to the latter assignment. First, the CT2 band is dominant in the UV-Vis extinction spectra of well-crystallized hematite,^{34,42,88,89} which is inconsistent with the weaker oscillator strengths of the formally forbidden LF transitions. Second, the CT1 and CT2 bands perfectly match the features in the O K-edge emission spectra of $\alpha\text{-Fe}_2\text{O}_3$,^{29,59,92} namely, the maximum at $\sim 525.5 \text{ eV}$ and a shoulder at $\sim 527.5 \text{ eV}$, respectively. Thus, the CT2 band is due to the O 2p–Fe 3d charge transfer, in agreement with ref. 34,84,86,93–97.

The observed decrease in energy of the CT1 and CT2 transitions as well as the intensity redistribution between them with increasing NP size can be correlated with restoration of the hematite-like local symmetry, which is accompanied by an increase in the antiferromagnetic coupling. Indeed, except for $\text{Fe}(\text{H}_2\text{O})_6^{3+}$, paramagnetic monomeric Fe^{3+} aqua hydroxo complexes are characterized by two OH 2p–Fe 3d CT transitions at 205–245 and 295–335 nm.⁹⁸ Similarly, the CT transitions are at 218 and 280 nm in the FeO_6^{9-} groups dissolved in MgO .⁹⁹ However, these bands red shift, respectively, to 245–260 and 335 nm in spectra of spin-paired ferric hydroxide clusters immersed in water,⁹⁸ zeolites,¹⁰⁰ and $\text{CaO-Fe}_2\text{O}_3\text{-P}_2\text{O}_5/\text{SiO}_2$ slags.¹⁰¹ In the limiting case of well-crystallized hematite, they are at ~ 270 and 430 nm , respectively.^{34,42,88,89} It is worth noting that the CT1 transition has higher intensity compared to the CT2 transition in the spectra of ferric hydroxide clusters but the intensity pattern is reverse in the energy losses spectra of bulk hematite. The reason can be contribution of tetrahedrally (T_d) or defectively coordinated ferric cations to the CT1 band, which increases with decreasing size of hematite NPs.²⁸ In fact, a strong CT band at $\sim 218\text{--}230 \text{ nm}$ was assigned to Fe^{3+} ions either in tetrahedral coordination⁹⁶ (T_d) or in a defective

environment^{100,102} in silicates. A larger HOMO–LUMO gap of metal centered tetrahedra compared to octahedra is predicted by molecular orbital calculations.¹⁰³

The remaining weak bands 1–7 have previously been attributed to the LF transitions,^{58,67,86} the p–d and d–d CT transitions,^{34,60,96} and oxygen vacancies,¹⁰⁴ while band 1' at $\sim 515 \text{ nm}$ has not previously been noticed (Table S2, ESI†). To clarify the band assignment, the impact of NP size on the band positions and intensities in the second derivative spectra was examined. As seen from Fig. 4 and Table S2 (ESI†), bands 1 and 2 at ~ 540 and 486 nm , respectively, practically *do not shift* as NP size increases up to 60 nm . The same effect was reported for NPs synthesized through a thermal route.⁷⁴ At the same time, bands 3, 5, and 6 red shift by 7–10 nm, which is much less significant compared to the CT1 (by 35 nm) and CT2 (by 25 nm) bands. The weak dependence on the NP size is inconsistent with the suggested³⁴ CT origin for bands 1–7 and the O-vacancy origin¹⁰⁴ for band 1 but supports their earlier assignment^{58,67} to the LF transitions. Hence, the intensity increase of these bands with increasing NPs can be related to overlapping between Fe 3d and O 2p orbitals which relaxes the Laporte rule.⁵⁸

Because of the lack of consensus in the literature on assignment of bands 1–7 to particular LF transitions (Table S2, ESI†), this problem was revisited in ESI†. For example, we attribute band 1' at $\sim 515 \text{ nm}$ to the LF transitions in the T_d sites. An increase in the band intensity with decreasing NP size suggests that concentration of such sites increases as NPs become smaller. Interestingly, band 1' is also observed in the spectrum of FH (Fig. 4), implying the presence of T_d sites in this polymorph. Based on our assignment of the LF bands and energy of the ${}^6A_1 \rightarrow {}^4T_1$ (4G) transitions of $11\,710 \text{ cm}^{-1}$ (ref. 77) we obtain a value of $1.38 \pm 0.2 \text{ eV}$ for the ligand

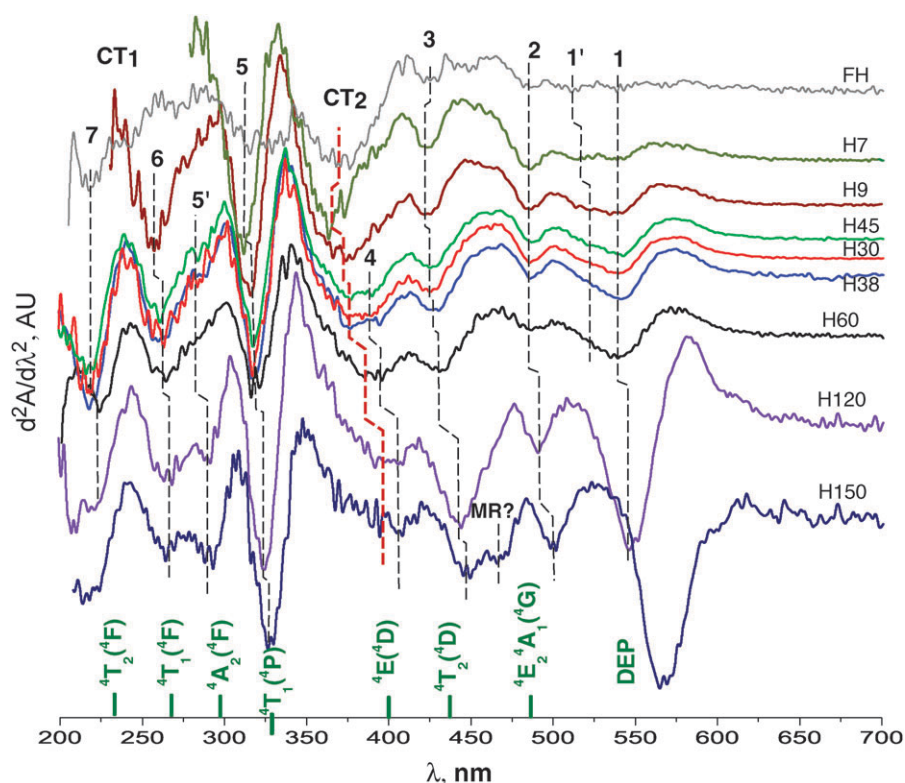


Fig. 4 Second derivative of UV-Vis absorption spectra of aqueous suspensions of hematite and FH NPs shown in Fig. 3a. From top to bottom: FH (grey), H7 (olive), H9 (wine), H30 (red), H45 (green), H38 (blue), H60 (black), H120 (violet), and H150 (navy). In the bottom part are shown the spectroscopic terms and positions of quartet LF states calculated using the Tanabe-Sugano diagram for $3d^5$ high-spin configuration with Racah parameter $B = 636 \text{ cm}^{-1}$ and $C/B = 4.48$. MR = Mie resonance. Broken vertical lines are guiding eye to show size-driven shifts of the peak positions.

field splitting $10 Dq$ in 38 nm hematite. This value is in excellent agreement with a value of 1.37 eV measured directly by X-ray absorption spectroscopy (XAS) for similarly synthesized 30 nm hematite.⁵⁹

Finally, electronic absorption of paramagnetic FH NPs (Fig. 3) consists of only two strong bands centered at $<200 \text{ nm}$ and $\sim 330 \text{ nm}$. This spectrum is very similar to the spectra of paramagnetic akageneite ($\beta\text{-FeOOH}$).^{105,106} Both the bands are assignable to the CT transitions in weakly antiferromagnetically coupled ferric octahedra.⁹⁸ On the other hand, the deconvoluted bands in the spectrum of FH, including band 1', are the same as in the spectrum of H7 (Fig. 4 and Table S2, ESI†). These observations imply similarities in the lattice structures of FH, akageneite, and H7, including the presence of tetrahedrally coordinated ferric ions.

XPS characterization of Fe–O bond covalency

To directly probe changes in valence electron population of oxygen with increasing NP size, the method of relative Auger KLL oxygen energies^{107,108} is used in the present work. This approach is based on the trend of separation between the $KL_{23}L_{23}$ and KL_1L_{23} O lines to increase with decreasing ionic character of the metal–oxygen bonds. The advantage of this approach over other XPS-based methods is its independence of variations in Madelung potential, Fermi level, and relaxation effects¹⁰⁹ with NP size as well as of the final-state effects caused by the core hole screening.^{29–31} The O KLL Auger

electron spectra of FH and hematite NPs and the peak assignment are shown in Fig. 5. As seen from Fig. 5, the center of gravity of the KL_1L_{23} line monotonically shifts farther from the $KL_{23}L_{23}$ line as NP size increases, if the contribution of the surface/interior hydroxyls at $\sim 488 \text{ eV}$ to the line shape is neglected. Though the shifts in the line position with NP size are subtle, they were reproduced in duplicate measurements. This observation confirms the UV-Vis spectra-based conclusion that the net Fe–O bond covalency increases with increasing NP size. However, as follows from our results and published data,⁵⁹ X-ray based spectroscopies are less sensitive to the NP size-induced changes in electronic properties of hematite compared to the optical absorption method.

Optical energy gap

The Tauc–Mott (TM) plots derived from the absorption spectra are used to determine the type and value of the optical gaps of hematite NPs in suspensions. The TM approximation of the absorption edge of an amorphous semiconductor is^{110,111}

$$(\alpha E_{\text{ph}})^n = B(E_{\text{ph}} - E_g) \quad (1)$$

where α is the absorption coefficient, E_g is the optical energy gap, B is a constant, E_{ph} is the photon energy ($E_{\text{ph}} = h\nu$) of the incident light, and n is an index characterizing the type of optical transition: n equals 2 for allowed direct transition and

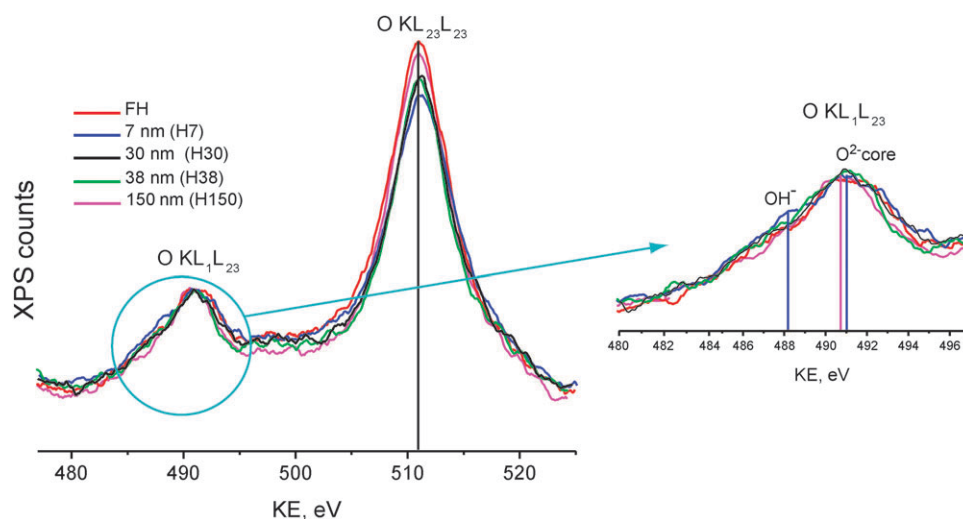


Fig. 5 O KLL Auger spectra of hematite NPs. The spectra were shifted to the same position of the $KL_{23}L_{23}$ line and normalized to the same intensity of the KL_1L_{23} line. KE = kinetic energy.

0.5 for allowed indirect transitions. Relationship (1) assumes that (a) dispersion of the refractive index of the material near the absorption edge can be neglected and (b) the conduction and valence band edges are parabolic functions of the momentum and is only valid for photon energies exceeding the band gap where this approximation holds. The optical band gaps are obtained from the intercept of the best linear parts of the curves near the band edge with $(\alpha E_{ph})^n = 0$. In the case of films, the absorption coefficient α is defined by the Beer–Bouger–Lambert law as $\alpha = A/d$, where A is the optical absorbance and d is the film thickness. However, this parameter cannot be determined in the case of suspensions of NPs. Instead, we used $\alpha = A/c$, where c is concentration of NPs in $g\ l^{-1}$.

The TM plots for the baseline corrected spectra (Fig. 3b) are shown in Fig. 6. The resulting band gap values are plotted as a function of NP size in Fig. 7. For comparison, the deflection points of the absorption spectra were also determined. As seen from Fig. 6, except for H150, the band gap is described better using the *direct allowed* than indirect allowed model. Both the direct and indirect band gaps decrease with increasing NP size

(Fig. 7). The slope of both the dependences abruptly increases at H150, which is due to the optical distortions (*vide supra*). As expected, the direct band gap is much more sensitive to NP size than both the indirect band gap and the deflection point since the latter two approximate energy of the DEP transition. The obtained values of the direct band gap of 2.18–2.95 eV for NPs of 120 nm size and smaller correspond well to values of 2–3 eV reported for the direct band gap of nanoparticulate hematite^{35–43,73} as well as for the onset of photoresponse of nanoparticulate hematite films.^{35,36,49–52}

It is interesting to note that the slope of the NP size dependence of the direct band gap slightly increases at NP sizes smaller than ~ 40 nm. Assuming that the 10 nm estimation of the radius of the first Bohr exciton^{18,24} is inaccurate, one might speculate that the additional enlargement of the band gap is provided by the quantum confinement (QC) effect. However, this conclusion would be ambiguous at this stage, since stoichiometry and lattice order of hematite vary non-linearly with NP size and mask QC, if any.

Finally, it is instructive to compare rates of the direct band-gap closing for hematite and other transition metal

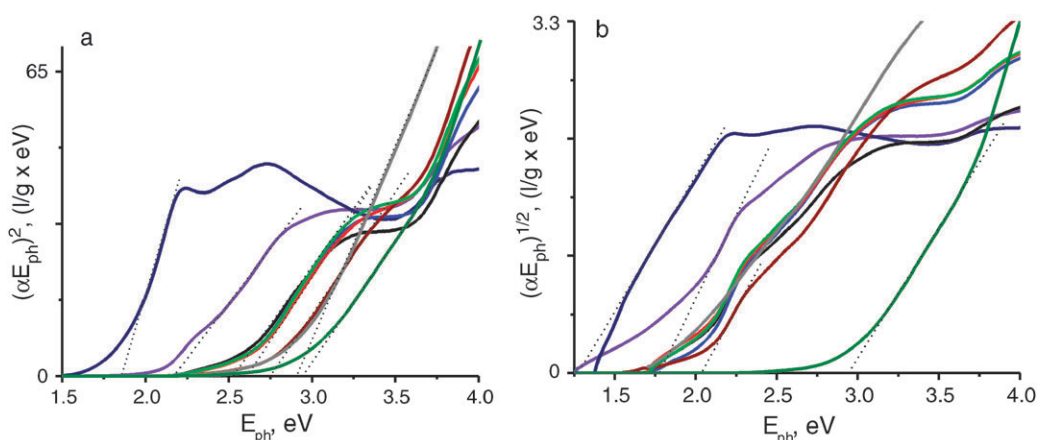


Fig. 6 TM plots for (a) direct and (b) indirect band gap of hematite NPs based on spectra shown in Fig. 3b. FH (grey), H7 (olive), H9 (wine), H30 (red), H45 (green), H38 (blue), H60 (black), H120 (violet), and H150 (navy).

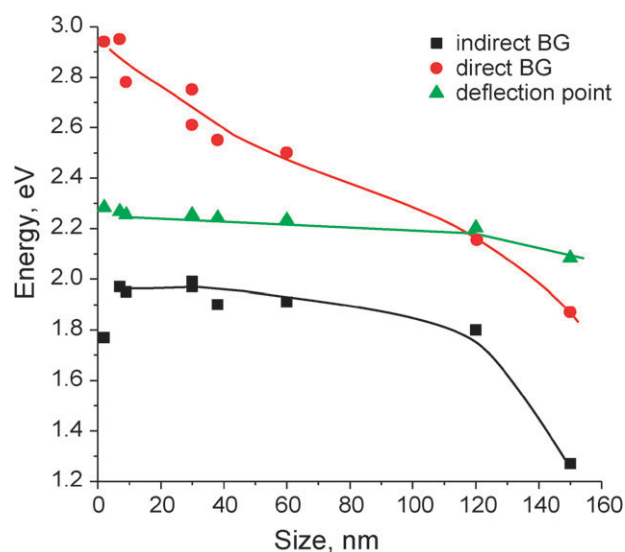


Fig. 7 NP size dependence of (circle) direct band gap, (square) indirect band gap and (triangle) deflection point for hematite NPs in suspensions. Estimated error in energies < 0.05 eV.

oxides. The value of $\sim 7 \times 10^{-3}$ eV nm $^{-1}$ found for hematite NPs in the 7–120 nm size range is much smaller compared to that of ZnO in the QC regime ($\sim 7 \times 10^{-2}$ eV nm $^{-1}$ in the 7–3 nm size range).^{112,113} At the same time, no change in the band gap for sizes in the 2–27 nm range compared to bulk was observed for anatase,¹¹⁴ which suggests high structural stability of this titania polymorph.

Discussion

The origin of the energy gap and the gap dependence on NP size

Using NP size of hematite as a variable, we found that the direct O 2p–Fe 3d CT transitions dominate at the absorption edge of this oxide. This result is at odds with the conventional LF view-point^{1,49,50,53,56–60} but supports the classification of hematite as a CT magnetic insulator.^{29–33,44,92} In the CT insulators, the top of the valence band has primarily oxygen 2p non-bonding character, while the conduction band mainly arises from the Fe 3d antibonding t_{2g} orbitals. Thus, both photoexcitation with visible light and p-doping of hematite give rise to delocalized O 2p holes, implying that the insulating energy gap of hematite is indeed the band gap.

The CT origin of the gap allows attributing the observed band-gap opening by ~ 0.8 eV with decreasing NP size in the 120–7 nm range (Fig. 7) to weakening of the Fe 3d–O 2p hybridization in the dominating O_h sites and to the formation of the T_d sites. The former effect manifests itself as a decrease in (i) intensities of the CT2 and LF bands in the optical absorption spectra, (ii) separation between the $KL_{23}L_{23}$ and KL_1L_{23} O Auger lines in the XPS spectra, and, as already reported,⁵⁹ (iii) a decrease in the pre-edge peak at the O 1s threshold in the XAS spectra. The lower overlap of the Fe 3d and O 2p orbitals in smaller hematite NPs probably stems from an increase in concentration of iron vacancies, which is accompanied by an increase in the a and c cell parameters, lattice disorder, and relaxation of trigonal distortion of the O_h

symmetry of ferric octahedra.^{1,58,67,75,115,116} In fact, incorporation of charge-compensating protons at iron vacancies is equivalent to substitution of O^{2-} by more electronegative OH^- ligands. Along with the creation of the iron vacancies, such substitution increases ionicity of the Fe–O bonds and suppresses intersite electronic coupling. An additional contribution to the opening of the Fe 3d–O 2p band gap is expected from a lower number of Fe atoms that coordinate to the O atom, which decreases the available unoccupied density of states (available from empty Fe 3d bands). Another consequence of the decreased Fe 3d–O 2p hybridization and iron deficiency is destabilization of the valence band edge.^{61,103} Finally, it is worth noting that the T_d sites, despite having shorter Fe–O bonds and stronger Fe 3d–O 2p hybridization compared to the O_h sites,⁶⁷ are characterized by wider HOMO–LUMO gaps.¹⁰³ The presence of such sites probably decreases the intersite electron coupling leading to a decrease in the average Fe 3d–O 2p hybridization. However, this effect as well as positions of the electronic energy levels of the T_d sites in the energy structure of iron-deficient hematite and FH NPs requires further theoretical modeling.

Contribution of LF transitions to the electronic properties of hematite

Based on the effect of NP size on the band intensities and positions, the ligand-field (LF) absorption bands have been differentiated from the CT absorption bands and reassigned using the Tanabe–Sugano (TS) correlation diagram (Table S2, ESI†). Interestingly, at variance with the higher-lying LF states, energies of the DEP (band 1) and the $^4E, ^4A_1(^4G)$ spin flip transitions (band 2) practically do not change with NP size in the 7–60 nm range (Table S2, ESI†). This feature can be ascribed to (1) strong localization of the corresponding excitations, (2) a weak dependence of the exchange energy on both the Fe–O bond length and the structural rearrangement of the FeO_6 octahedra^{34,117} and, in case of DEP, (3) the low sensitivity of the LF splitting parameter to NP size of hematite.⁶⁴

The reasons for the larger red shifts of the higher-energy LF bands 3–7 are not clear at the moment. These shifts can tentatively be ascribed to certain delocalization of the corresponding intra-atomic d–d excitations by mixing with the superimposed CT bands. This can happen due to increased 3d–2p hybridization and/or screening of the exchange repulsion by the more delocalized proximate oxygen hole created by the CT event. As matter of fact, the influence of the CT effects beyond the first coordination sphere on the LF transitions is known.¹¹⁸ Excitation of the CT bands results in the population of the excited LF states, which may then decay through typical d–d photochemical pathways.¹¹⁹ Hence, the coupling between the LF and CT excitations provides an additional, highly efficient deactivation pathway for the CT states in hematite. In fact, ultra-fast kinetics of energy decay of CT excitations can be attributed to trapping of carriers by the strongly localized d–d levels,^{65,84,85} which substantially reduces carrier mobility. Since the on-site LF excitations do not directly create holes^{56,65} and are strongly coupled with phonons,⁶⁵ their presence within the band gap may explain

quenching of the band-gap emission by coarse hematite particles as well as the short diffusion length of the O 2p holes.

Comparison with previous results

The strong blue shift of the absorption edge observed with decreasing NP size in the present work agrees with previous results based on measurements of optical absorption,^{9,73} diffuse reflectance (DR) of NPs embedded in transparent matrix,^{52,56,72} DR of NPs as such,⁷¹ and cathodoluminescence.⁶⁰ However, our data contradict to the studies where no shift⁵⁹ or the opposite trend⁷⁵ was observed using the DR method without optical dilution. This discrepancy is explained by the optical distortions of the absorption edge in the latter case, which makes this technique inapplicable to measuring the band gap energies of highly refracting semiconducting NPs.⁷⁷ The earlier erroneous classification of the insulating gap of hematite as indirect can be attributed to measurements restricted to the vicinity of the DEP transition,⁵⁷ incorrect application of the TM technique,⁵⁰ or a lack of comparison with the direct band gap TM plots.^{62,63}

The intensity loss at the CT2 maximum in the X-ray emission spectrum (XES) excited in the vicinity of the O K-edge absorption threshold (530 eV) was also considered as evidence of the indirect character of the band gap of hematite.⁵⁹ In doing so, analogy with IIIA nitrides was used. Indeed, in the case of GaN, which has the direct band gap, emission at the highest energy is observed at excitation into the conduction band minimum.¹²⁰ This effect manifests itself as a shift of the emission peak to a higher energy. AlN (the indirect band gap) demonstrates the opposite trend. At the same time, hematite NPs exhibit *no* shift in the peak positions with

changing excitation energy.⁵⁹ Instead, there is a decrease in intensity of *both* the higher- and lower-energy shoulders of the main emission peak which are produced by splitting of the O 2p band by the Fe 3d–O 2p hybridization. Hence, taking into account the much more complicated electronic structure of hematite when compared to IIIA nitrides and the complexity caused by the core hole involved in the emission process in hematite,^{29–31} one can suggest that the dependence of the XES of hematite on the excitation energy may be driven by other mechanisms, other than the indirect band gap, which requires further studies.

Dependence of aquatic chemistry of ferric (hydr)oxides on NP size

Narrower band gaps and lower energy of the valence band edges (Fig. 8) imply a higher electron affinity (defined as the energy difference between the vacuum level and the bottom of the conduction band) of larger hematite NPs and higher oxidation power of their thermalized or photogenerated holes. Along with lower mobility of charge carriers, this effect is the cause of the decrease in oxidative catalytic activity of hematite with decreasing NP size.⁵ Improved catalytic properties can be also behind higher cytotoxicity of larger hematite NPs. Higher electron affinity makes larger NPs stronger electron acceptors from reducing species⁵ including bacteria.¹¹ The NP-driven destabilization of energy of the conduction and valence bands (Fig. 8) is also consistent with the degradation of photocatalytic properties of hematite with decreasing NP size.^{6–8,74} Nanoparticulate hematite photoelectrodes characterized by a higher intensity and/or low energy of the CT2 band generally demonstrate better oxidative photocatalytic activity,^{49,52,87,121,122}

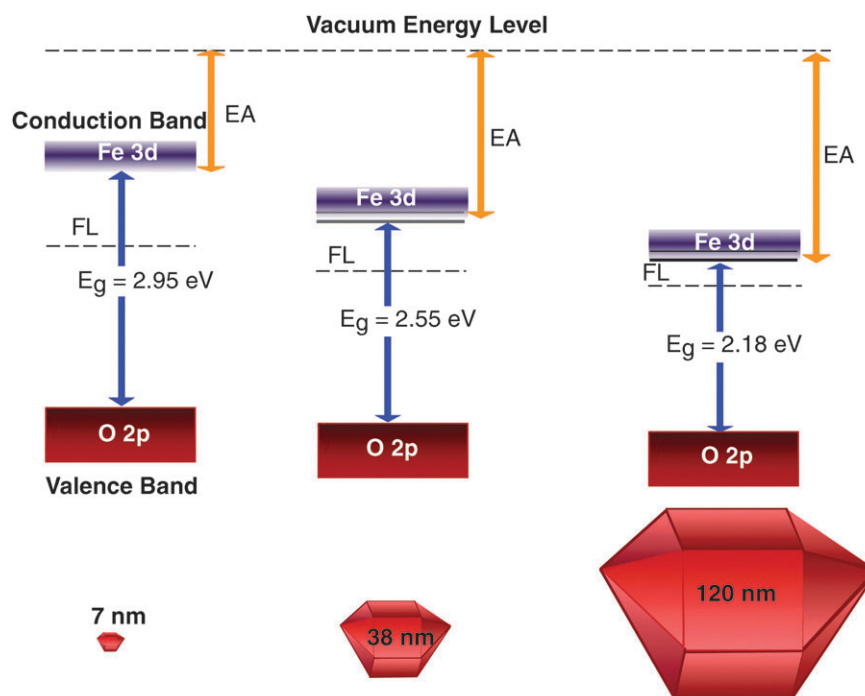


Fig. 8 Schematic diagram showing effect of NP size on electronic structure of hematite. EA = electron affinity, FL = Fermi level, E_g = band gap. Lines in the conduction band of 38 and 120 nm NPs represent the LF states. LF transitions become more forbidden with decreasing NP size, as schematized by vanishing contrast of the lines color.

though there are exceptions attributable to the presence of electron traps.¹²³ This correlation implies that the O 2p–Fe 3d charge transfer and its perturbation by the ligand field are among the primary controls of (photo)catalytic properties of hematite, along with concentration of free carriers, electron–hole recombination rate, concentration of suitable surface sites, and kinetics of charge transfer at the electrode–electrolyte interface.

The nanosize driven raise of the conduction band can be related to the observed decrease in the adsorption affinity and capacity of hematite towards Cu(II) and U(VI) ions (Fig. S1, ESI†). Indeed, it was recently shown that strong binding of Pb(II) ions to hematite is mediated by Fe 3d electrons,¹²⁴ suggesting electron donation to the conduction band. At the same time, the adsorption is weak on isostructural corundum (α -Al₂O₃) which has much higher energy of the conduction band. On the other hand, the increased ionicity of smaller NPs may also increase the sticking probability of polar molecules.²³ When such molecules approach the surface, their dipole moments interact with the electric field at the surface to orient the molecule, thus favoring attractive bonding interactions. Coupled with the enhanced Lewis basicity of surface oxygens, this effect is probably responsible for the fact that nanoparticulate hematite adsorbs CO₂ while coarse hematite particles do not.¹²⁵

Changes in chemical properties of other ferric (hydr)oxides with decreasing NP size have previously been discussed exclusively in terms of varying crystallographic facets,^{13,126} aggregation effects,¹⁰ or higher asperity.⁶⁴ However, lower intensity and energy of the CT transitions in optical spectra of goethite nanorods imply that the lower redox capacity of nanorods¹⁰ compared to microrods¹²⁷ stems, as in the case of hematite, from increased ionicity and destabilization of the conduction and valence bands of nanorods. The enhanced catalytic effect of aged FH suspensions on oxidation of ferrous iron by dissolved oxygen compared to the as-synthesized NPs¹²⁸ is understandable given that aged FH have larger sizes and are partially transformed into goethite.¹ These changes lead to narrowing band gaps and strengthening the O 2p–Fe 3d hybridization. Finally, the main reason for the increased reductive dissolution of smaller FH and goethite NPs by hydroquinone¹²⁹ can be a higher reductive potential of electrons injected into their conductive bands. Higher ionicity further enhances solubility of smaller NPs, in addition to the conventional effect of surface area.

Role of the Mie resonance in the photochemical properties of hematite

The Mie resonance, which is observed as extra extinction at $\lambda > 550$ nm for 150 nm hematite NPs (Fig. 3a), can also be observed for absorption spectra of strongly aggregated smaller NPs.⁷⁷ Since activation of this effect is accompanied by significant local enhancement of the electromagnetic field near the particle surface,¹³⁰ it can be considered as a new type of the CT excitation that propagates along the particle/aggregate surface or a CT surface resonance.^{90,130} The nature of this effect implies that it will have impact on photochemical performance of hematite NPs, which however has not been addressed so far.

First of all, the strong scattering component can be an additional channel of dissipation of the photon energy which contributes to the steeper onset of the absorption spectrum of nanoparticulate hematite photoelectrodes compared to their photoresponse.^{35,36,49–52} This effect has typically been ascribed to higher charge-separating efficiency of less-penetrating more energetic photons.^{51,53,131} Interestingly, the general trend in the design of hematite photoelectrodes is to match their feature size to the short diffusion length of holes.^{35,39,49,132} This design criterion results in non-spherical nanomorphologies of hematite NPs which do not support the formation of the surface modes¹³⁰ and hence minimize the energy losses due to light scattering. On the other hand, it is evident that Mie resonance can also improve the NP performance because it shifts the CT absorption to the visual range. Hence, controlling the propagation and damping of the surface resonance modes can open up new approaches for manipulating photochemical properties of hematite NPs.

Conclusions

Examination of the NP size effect on the UV-Vis absorption and XPS spectra of hematite NPs has resolved a number of uncertainties about the electronic and structural properties of this oxide. It was shown that

- (1) The insulating gap of hematite is generated by the direct interband O 2p–Fe 3d charge transfer process;
- (2) The band gap increases from 2.18 to 2.95 eV with decreasing NP size from 120 nm to 7 nm, which is attributed to an increase in the Fe–O covalency upon the size-drive restoration of the hematite lattice structure;
- (3) Ferric ions in tetrahedral or defected octahedral coordination are present in hematite NPs up to 60 nm size and ferrihydrite as well. These defects are characterized by larger HOMO–LUMO gaps. Concentration of such defective sites decreases, while crystallinity of hematite lattice increases with increasing NP size;
- (4) A manifold of weak bands superimposed onto two p–d CT bands is assigned to d–d LF transitions using the TS correlation diagram, which gave LF parameters $B = 640 \pm 10 \text{ cm}^{-1}$ and $10 Dq = 1.38 \pm 0.2 \text{ eV}$;
- (5) The Mie resonance significantly distorts the absorption edge of hematite NPs larger than ~ 120 nm;
- (6) Sensitivity of the UV-Vis absorption spectra to variations in both the band gap and electronic properties of hematite is higher compared to the X-ray based spectroscopies.

Acknowledgements

The NSF support under grants #0925232 and #0749461 is acknowledged. This work has used the shared experimental facilities that are supported primarily by the MRSEC program of NSF # DMR 0213574 and by the New York State Office of Science Technology and Academic Research (NYSTAR).

References

- 1 R. M. Cornell and U. Schwertmann, *The Iron Oxide: Structure, Properties, Reactions and Uses*, VCH, Weinheim, 1996.
- 2 S. Morup, D. E. Madsen, C. Frandsen, C. R. H. Bahl and M. F. Hansen, *J. Phys.: Condens. Matter*, 2007, **19**, 213202.

- 3 R. Zboril, M. Mashlan and D. Petridis, *Chem. Mater.*, 2002, **14**, 969–982.
- 4 J. P. Jolivet, E. Tronc and C. Chaneac, *C. R. Geosci.*, 2006, **338**, 488–497.
- 5 I. V. Chernyshova, S. Ponnuram and P. Somasundaran, *Effect of nanosize on redox properties of ferric (hydr)oxides: linking electronic and redox properties*, submitted.
- 6 Y. Wang, W. P. Du and Y. M. Xu, *Langmuir*, 2009, **25**, 2895–2899.
- 7 X. L. Fang, C. Chen, M. S. Jin, Q. Kuang, Z. X. Xie, S. Y. Xie, R. B. Huang and L. S. Zheng, *J. Mater. Chem.*, 2009, **19**, 6154–6160.
- 8 A. Ansari, J. Peral, X. Domenech, R. Rodriguezclemente, A. Roig and E. Molins, *J. Photochem. Photobiol., A*, 1995, **87**, 121–125.
- 9 S. Chatterjee, S. Sarkar and S. N. Bhattacharyya, *J. Photochem. Photobiol., A*, 1993, **72**, 183–187.
- 10 D. M. Cwiertny, R. M. Handler, M. V. Schaefer, V. H. Grassian and M. M. Scherer, *Geochim. Cosmochim. Acta*, 2008, **72**, 1365–1380.
- 11 S. Bose, M. F. Hochella, Y. A. Gorby, D. W. Kennedy, D. E. McCready, A. S. Madden and B. H. Lower, *Geochim. Cosmochim. Acta*, 2009, **73**, 962–976.
- 12 R. Wottrich, S. Diabate and H. F. Krug, *Int. J. Hyg. Environ. Health*, 2004, **207**, 353–361.
- 13 M. Villalobos, M. A. Cheney and J. Alcaraz-Cienfuegos, *J. Colloid Interface Sci.*, 2009, **336**, 412–422.
- 14 A. S. Madden, M. F. Hochella Jr and T. P. Luxton, *Geochim. Cosmochim. Acta*, 2006, **70**, 4095–4104.
- 15 H. Zeng, A. Singh, S. Basak, K. U. Ulrich, M. Sahu, P. Biswas, J. G. Catalano and D. E. Giammar, *Environ. Sci. Technol.*, 2009, **43**, 1373–1378.
- 16 M. Auffan, J. Rose, J. Y. Bottero, G. V. Lowry, J. P. Jolivet and M. R. Wiesner, *Nat. Nanotechnol.*, 2009, **4**, 634–641.
- 17 M. Calatayud, L. Maldonado and C. Minot, *J. Phys. Chem. C*, 2008, **112**, 16087–16095.
- 18 B. Gilbert and J. F. Banfield, in *Molecular Geomicrobiology*, 2005, vol. 59, pp. 109–155.
- 19 P. J. Vikesland, A. M. Heathcock, R. L. Rebodos and K. E. Makus, *Environ. Sci. Technol.*, 2007, **41**, 5277–5283.
- 20 L. Wang, L. X. Chang, B. Zhao, Z. Y. Yuan, G. S. Shao and W. J. Zheng, *Inorg. Chem.*, 2008, **47**, 1443–1452.
- 21 *Interface Science and Technology*, in *Surface Complexation Modeling*, ed. J. Lützenkirchen, Elsevier, Amsterdam, 2006, vol. 11.
- 22 C. A. Ohlin, E. M. Villa, J. R. Rustad and W. H. Casey, *Nat. Mater.*, 2010, **9**, 11–19.
- 23 H. H. Kung, *Transition Metal Oxides: Surface Chemistry and Catalysis*, Elsevier, New York, 1989.
- 24 N. J. Cherepy, D. B. Liston, J. A. Lovejoy, H. M. Deng and J. Z. Zhang, *J. Phys. Chem. B*, 1998, **102**, 770–776.
- 25 F. T. Parker, M. W. Foster, D. T. Margulies and A. E. Berkowitz, *Phys. Rev. B: Condens. Matter*, 1993, **47**, 7885–7891.
- 26 Z. Abbas, C. Labbez, S. Nordholm and E. Ahlberg, *J. Phys. Chem. C*, 2008, **112**, 5715–5723.
- 27 J. R. Rustad and A. R. Felmy, *Geochim. Cosmochim. Acta*, 2005, **69**, 1405–1411.
- 28 I. V. Chernyshova, M. F. Hochella and A. S. Madden, *Phys. Chem. Chem. Phys.*, 2007, **9**, 1736–1750.
- 29 G. Drager, W. Czolbe and J. A. Leiro, *Phys. Rev. B: Condens. Matter*, 1992, **45**, 8283–8287.
- 30 A. Fujimori, M. Saeki, N. Kimizuka, M. Taniguchi and S. Suga, *Phys. Rev. B: Condens. Matter*, 1986, **34**, 7318–7333.
- 31 R. J. Lad and V. E. Henrich, *Phys. Rev. B: Condens. Matter*, 1989, **39**, 13478–13485.
- 32 M. Catti, G. Valerio and R. Dovesi, *Phys. Rev. B: Condens. Matter*, 1995, **51**, 7441–7450.
- 33 A. E. Bocquet, T. Mizokawa, T. Saitoh, H. Namatame and A. Fujimori, *Phys. Rev. B: Condens. Matter*, 1992, **46**, 3771–3784.
- 34 R. V. Pisarev, A. S. Moskvina, A. M. Kalashnikova and T. Rasing, *Phys. Rev. B: Condens. Matter Mater. Phys.*, 2009, **79**, 235128.
- 35 N. Beermann, L. Vayssieres, S. E. Lindquist and A. Hagfeldt, *J. Electrochem. Soc.*, 2000, **147**, 2456–2461.
- 36 A. Kleiman-Shwarsctein, Y. S. Hu, A. J. Forman, G. D. Stucky and E. W. McFarland, *J. Phys. Chem. C*, 2008, **112**, 15900–15907.
- 37 R. Schrebler, K. Bello, F. Vera, P. Cury, E. Munoz, R. del Rio, H. G. Meier, R. Cordova and E. A. Dalchiele, *Electrochem. Solid-State Lett.*, 2006, **9**, C110–C113.
- 38 S. Saretni-Yarahmadi, K. G. U. Wijayantha, A. A. Tahir and B. Vaidhyanathan, *J. Phys. Chem. C*, 2009, **113**, 4768–4778.
- 39 A. A. Tahir, K. G. U. Wijayantha, S. Saremi-Yarahmadi, M. Mazhar and V. McKee, *Chem. Mater.*, 2009, **21**, 3763–3772.
- 40 L. Dghoughi, B. Elidrissi, C. Bernede, A. Addou, M. A. Lamrani, A. Regragui and H. Erguig, *Appl. Surf. Sci.*, 2006, **253**, 1823–1829.
- 41 W. B. Ingler, J. P. Baltrus and S. U. M. Khan, *J. Am. Chem. Soc.*, 2004, **126**, 10238–10239.
- 42 J. A. Glasscock, P. R. F. Barnes, I. C. Plumb, A. Bendavid and P. J. Martin, *Thin Solid Films*, 2008, **516**, 1716–1724.
- 43 J. G. Yu, X. X. Yu, B. B. Huang, X. Y. Zhang and Y. Dai, *Cryst. Growth Des.*, 2009, **9**, 1474–1480.
- 44 G. Rollmann, A. Rohrbach, P. Entel and J. Hafner, *Phys. Rev. B: Condens. Matter Mater. Phys.*, 2004, **69**, 165107.
- 45 N. C. Wilson and S. P. Russo, *Phys. Rev. B: Condens. Matter Mater. Phys.*, 2009, **79**, 094113.
- 46 Y. Yamanoi, S. Nakashima and M. Katsura, *Am. Mineral.*, 2009, **94**, 90–97.
- 47 W. C. Mackrodt, F. Jollet and M. Gautier-Soyer, *Philos. Mag. B*, 1999, **79**, 25–36.
- 48 J. I. Pankove, *Optical Properties in Semiconductors*, Dover Publications, New York, 1971.
- 49 A. Duret and M. Gratzel, *J. Phys. Chem. B*, 2005, **109**, 17184–17191.
- 50 J. H. Kennedy and K. W. Frese, *J. Electrochem. Soc.*, 1978, **125**, 709–714.
- 51 I. Cesar, K. Sivula, A. Kay, R. Zboril and M. Graetzel, *J. Phys. Chem. C*, 2009, **113**, 772–782.
- 52 K. Cheng, Y. P. He, Y. M. Miao, B. S. Zou, Y. G. Wang, T. H. Wang, X. T. Zhang and Z. L. Du, *J. Phys. Chem. B*, 2006, **110**, 7259–7264.
- 53 A. Kay, I. Cesar and M. Gratzel, *J. Am. Chem. Soc.*, 2006, **128**, 15714–15721.
- 54 B. S. Zou and V. Volkov, *J. Phys. Chem. Solids*, 2000, **61**, 757–764.
- 55 C. Gleitzer, in *Electrical properties of oxide materials, key engineering materials*, ed. J. Nowotny and C. C. Sorrell, Trans Tech, Switzerland, 1997, vol. 125–126, pp. 355–417.
- 56 Y. P. He, Y. M. Miao, C. R. Li, S. Q. Wang, L. Cao, S. S. Xie, G. Z. Yang, B. S. Zou and C. Burda, *Phys. Rev. B: Condens. Matter Mater. Phys.*, 2005, **71**, 125411.
- 57 M. P. Dareedwards, J. B. Goodenough, A. Hamnett and P. R. Trevellick, *J. Chem. Soc., Faraday Trans. I*, 1983, **79**, 2027–2041.
- 58 D. M. Sherman and T. D. Waite, *Am. Mineral.*, 1985, **70**, 1262–1269.
- 59 B. Gilbert, C. Frandsen, E. R. Maxey and D. M. Sherman, *Phys. Rev. B: Condens. Matter*, 2009, **79**, 035108.
- 60 C. Díaz-Guerra, M. F. Chioncel and J. Piqueras, *Superlattices Microstruct.*, 2009, **45**, 145–150.
- 61 Y. Matsumoto, *J. Solid State Chem.*, 1996, **126**, 227–234.
- 62 S. Mohanty and J. Ghose, *J. Phys. Chem. Solids*, 1992, **53**, 81–91.
- 63 E. Pollert, J. Hejtmánek, J. P. Doumerc, J. C. Launay and P. Hagenmüller, *Z. Anorg. Allg. Chem.*, 1985, **528**, 202–208.
- 64 B. Gilbert, C. Frandsen, E. R. Maxey and D. M. Sherman, *Phys. Rev. B: Condens. Matter*, 2009, **79**, 035108.
- 65 T. Y. Chen, C. H. Hsia, H. S. Son and D. H. Son, *J. Am. Chem. Soc.*, 2007, **129**, 10829–10836.
- 66 T. Hashimoto, T. Yamada and T. Yoko, *J. Appl. Phys.*, 1996, **80**, 3184–3190.
- 67 D. M. Sherman, *Phys. Chem. Miner.*, 1985, **12**, 161–175.
- 68 M. Lenglet, F. Hochu and Z. Simsa, *Mater. Res. Bull.*, 1998, **33**, 1821–1833.
- 69 M. Z. Dang, D. G. Rancourt, J. E. Dutrizac, G. Lamarche and R. Provencher, *Hyperfine Interact.*, 1998, **117**, 271–319.
- 70 P. A. Cox, *Transition Metal Oxides*, Clarendon Press, Oxford, 1992.
- 71 L. Lu, L. P. Li, X. J. Wang and G. S. Li, *J. Phys. Chem. B*, 2005, **109**, 17151–17156.
- 72 J. Torrent and V. Barron, *Clays Clay Miner.*, 2003, **51**, 309–317.

- 73 S. Zeng, K. Tang and T. Li, *J. Colloid Interface Sci.*, 2007, **312**, 513–521.
- 74 K. Sivula, R. Zboril, F. Le Formal, R. Robert, A. Weidenkaff, J. Tucek, J. Frydrych and M. Gratzel, *J. Am. Chem. Soc.*, 2010, **132**, 7436–7444.
- 75 N. Pailhe, A. Wattiaux, M. Gaudon and A. Demourgues, *J. Solid State Chem.*, 2008, **181**, 2697–2704.
- 76 B. S. Zou, W. Huang, M. Y. Han, S. F. Y. Li, X. C. Wu, Y. Zhang, J. S. Zhang, P. F. Wu and R. Y. Wang, *J. Phys. Chem. Solids*, 1997, **58**, 1315–1320.
- 77 I. V. Chernyshova, S. Ponnuram and P. Somasundaran, *Artifacts in measurements of optical band gaps of semiconducting nanoparticles by diffuse reflectance method*, (under preparation).
- 78 F. M. Michel, L. Ehm, S. M. Antao, P. L. Lee, P. J. Chupas, G. Liu, D. R. Strongin, M. A. A. Schoonen, B. L. Phillips and J. B. Parise, *Science*, 2007, **316**, 1726–1729.
- 79 F. M. Michel, V. Barron, J. Torrent, M. P. Morales, C. J. Serna, J. F. Boily, Q. S. Liu, A. Ambrosini, A. C. Cismasu and G. E. Brown, *Proc. Natl. Acad. Sci. U. S. A.*, 2010, **107**, 2787–2792.
- 80 D. Carta, M. F. Casula, A. Corrias, A. Falqui, G. Navarra and G. Pinna, *Mater. Chem. Phys.*, 2009, **113**, 349–355.
- 81 D. E. Janney, J. M. Cowley and P. R. Buseck, *Clays Clay Miner.*, 2000, **48**, 111–119.
- 82 E. Wolska and W. Szajda, *J. Mater. Sci.*, 1985, **20**, 4407–4412.
- 83 A. Bedidi and B. Cervelle, *J. Geophys. Res.*, 1993, **98**, 11941–11952.
- 84 H. M. Fan, G. J. You, Y. Li, Z. Zheng, H. R. Tan, Z. X. Shen, S. H. Tang and Y. P. Feng, *J. Phys. Chem. C*, 2009, **113**, 9928–9935.
- 85 A. G. Joly, J. R. Williams, S. A. Chambers, G. Xiong, W. P. Hess and D. M. Laman, *J. Appl. Phys.*, 2006, **99**, 053521.
- 86 L. A. Marusak, R. Messier and W. B. White, *J. Phys. Chem. Solids*, 1980, **41**, 981–984.
- 87 F. L. Souza, K. P. Lopes, P. A. P. Nascente and E. R. Leite, *Sol. Energy Mater. Sol. Cells*, 2009, **93**, 362–368.
- 88 A. I. Galuza, V. V. Eremenko and A. P. Kirichenko, *Fiz. Tverd. Tela*, 1979, **21**, 1125–1129.
- 89 C. T. Chen and B. D. Cahan, *J. Opt. Soc. Am.*, 1981, **71**, 932–934.
- 90 W. P. Hsu and E. Matijevic, *Appl. Opt.*, 1985, **24**, 1623–1630.
- 91 S. S. Wong and L. E. Brus, *J. Phys. Chem. B*, 2001, **105**, 599–603.
- 92 Y. Ma, P. D. Johnson, N. Wassdahl, J. Guo, P. Skytt, J. Nordgren, S. D. Kevan, J. E. Rubensson, T. Boske and W. Eberhardt, *Phys. Rev. B: Condens. Matter*, 1993, **48**, 2109–2111.
- 93 N. C. Debnath and A. B. Anderson, *J. Electrochem. Soc.*, 1982, **129**, 2169–2174.
- 94 R. F. G. Gardner, D. W. Tanner and F. Sweett, *J. Phys. Chem. Solids*, 1963, **24**, 1183.
- 95 T. Hashimoto, T. Yoko and S. Sakka, *J. Ceram. Soc. Jpn.*, 1993, **101**, 64–68.
- 96 L. Armelao, M. Bettinelli, M. Casarin, G. Granozzi, E. Tondello and A. Vittadini, *J. Phys.: Condens. Matter*, 1995, **7**, L299–L305.
- 97 K. A. Wickersheim and R. A. Lefever, *J. Chem. Phys.*, 1962, **36**, 844.
- 98 L. Lopes, J. de Laat and B. Legube, *Inorg. Chem.*, 2002, **41**, 2505–2517.
- 99 J. C. Cheng and J. C. Kemp, *Phys. Rev. B: Solid State*, 1971, **4**, 2841.
- 100 L. D. Li, Q. Shen, J. J. Li, Z. P. Hao, Z. P. Xu and G. Q. M. Lu, *Appl. Catal., A*, 2008, **344**, 131–141.
- 101 I. Zebger, F. Pfeifer and N. Nowack, *J. Non-Cryst. Solids*, 2005, **351**, 3443–3457.
- 102 A. Gervasini, C. Messi, P. Carniti, A. Ponti, N. Ravasio and F. Zaccaria, *J. Catal.*, 2009, **262**, 224–234.
- 103 P. M. Woodward, H. Mizoguchi, Y.-I. Kim and M. W. Stoltzfus, in *Metal Oxides: Chemistry and Applications*, ed. J. L. G. Fierro, CRC Press/Taylor & Francis Group, Boca Raton, FL, 2006, p. 783.
- 104 S. R. Basu, L. W. Martin, Y. H. Chu, M. Gajek, R. Ramesh, R. C. Rai, X. Xu and J. L. Musfeldt, *Appl. Phys. Lett.*, 2008, **92**, 091905.
- 105 A. Kumar and A. Singhal, *Nanotechnology*, 2007, **18**, 7.
- 106 A. G. Joly, G. Xiong, C. M. Wang, D. E. McCready, K. M. Beck and W. P. Hess, *Appl. Phys. Lett.*, 2007, **90**, 103504.
- 107 C. D. Wagner, D. A. Zatko and R. H. Raymond, *Anal. Chem.*, 1980, **52**, 1445–1451.
- 108 P. Ascarelli and G. Moretti, *Surf. Interface Anal.*, 1985, **7**, 8–12.
- 109 J. van den Brand, P. C. Snijders, W. G. Sloof, H. Terryn and J. H. W. de Wit, *J. Phys. Chem. B*, 2004, **108**, 6017–6024.
- 110 E. A. Davis and N. F. Mott, *Electronic Processes in Noncrystalline Materials*, Clarendon, Oxford, 1979.
- 111 J. Tauc, *Optical Properties of Solids*, Plenum, New York, 1969.
- 112 R. Viswanatha, S. Sapra, B. Satpati, P. V. Satyam, B. N. Dev and D. D. Sarma, *J. Mater. Chem.*, 2004, **14**, 661–668.
- 113 Y. S. Wang, P. J. Thomas and P. O'Brien, *J. Phys. Chem. B*, 2006, **110**, 4099–4104.
- 114 N. Serpone, D. Lawless and R. Khairutdinov, *J. Phys. Chem.*, 1995, **99**, 16646–16654.
- 115 U. Schwertmann and R. M. Cornell, *Iron oxides in the laboratory: preparation and characterization*, Wiley-VCH Weinheim, New York, 2000.
- 116 M. Blanchard, G. Morin, M. Lazzeri and E. Balan, *Geochim. Cosmochim. Acta*, 2010, **74**, 3948–3962.
- 117 J. Kunes, A. V. Lukyanov, V. I. Anisimov, R. T. Scalettar and W. E. Pickett, *Nat. Mater.*, 2008, **7**, 198–202.
- 118 M. Atanasov and D. Reinen, *J. Electron Spectrosc. Relat. Phenom.*, 1997, **86**, 185–199.
- 119 O. Horvath and K. L. Stevenson, *Charge Transfer Photochemistry of Coordination Compounds*, VCH Publishers, Inc., New York, 1993.
- 120 S. Eisebitt and W. Eberhardt, *J. Electron Spectrosc. Relat. Phenom.*, 2000, **110**, 335–358.
- 121 R. R. Rangaraju, A. Panday, K. S. Raja and M. Misra, *J. Phys. D: Appl. Phys.*, 2009, **42**, 135303.
- 122 S. Kakuta and T. Abe, *J. Mater. Sci.*, 2009, **44**, 2890–2898.
- 123 F. L. Souza, K. P. Lopes, E. Longo and E. R. Leite, *Phys. Chem. Chem. Phys.*, 2009, **11**, 1215–1219.
- 124 S. E. Mason, C. R. Iceman, K. S. Tanwar, T. P. Trainor and A. M. Chaka, *J. Phys. Chem. C*, 2009, **113**, 2159–2170.
- 125 C. H. Rochester and S. A. Topham, *J. Chem. Soc., Faraday Trans. 1*, 1979, **75**, 259–1267.
- 126 M. Villalobos, M. A. Trotz and J. O. Leckie, *J. Colloid Interface Sci.*, 2003, **268**, 273–287.
- 127 D. M. Cwiertny, G. J. Hunter, J. M. Pettibone, M. M. Scherer and V. H. Grassian, *J. Phys. Chem. C*, 2009, **113**, 2175–2186.
- 128 N. Tufekci and H. Z. Sarikaya, *Water Sci. Technol.*, 1998, **38**, 129–137.
- 129 A. J. Anschutz and R. L. Penn, *Geochem. Trans.*, 2005, **6**, 60–66.
- 130 P. Chylek, *J. Opt. Soc. Am.*, 1976, **66**, 285–287.
- 131 U. Bjorksten, J. Moser and M. Gratzel, *Chem. Mater.*, 1994, **6**, 858–863.
- 132 S. K. Mohapatra, S. E. John, S. Banerjee and M. Misra, *Chem. Mater.*, 2009, **21**, 3048–3055.